

PAPER

CaviPlasma: parametric study of discharge parameters of high-throughput water plasma treatment technology in glow-like discharge regime

To cite this article: J Čech *et al* 2024 *Plasma Sources Sci. Technol.* **33** 115005

View the [article online](#) for updates and enhancements.

You may also like

- [Effects of rose bengal on cavitation generation in gel phantom investigated using high-speed camera](#)
Jun Yasuda, Takuya Miyashita, Shin Yoshizawa *et al.*
- [Structural and Electrical Characterization of Cadmium Phosphate Glasses Doped with Different Concentration of Sodium Chloride](#)
Ghada A. I. Assayed, Adel Shaheen, Ammar Alsoud *et al.*
- [Quantitative assessment of reactive oxygen sonochemically generated by cavitation bubbles](#)
Jun Yasuda, Takuya Miyashita, Kei Taguchi *et al.*



HIDEN ANALYTICAL

Analysis Solutions for your Plasma Research

For Surface Science

- ▶ Surface Analysis
- ▶ SIMS
- ▶ 3D depth Profiling
- ▶ Nanometre depth resolution

■ Compact SIMS

■ SIMS Workstation

■ Auto SIMS

For Plasma Diagnostics

- ▶ Plasma characterisation
- ▶ Customised systems to suit plasma Configuration
- ▶ Mass and energy analysis of plasma ions
- ▶ Characterisation of neutrals and radicals

■ ESPion

■ HPR-60 MBMS

■ EQP Series

Click to view our product catalogue

■ Knowledge ■ Experience ■ Expertise

Contact Hiden Analytical for further details:
W www.HidenAnalytical.com
E info@hiden.co.uk

CaviPlasma: parametric study of discharge parameters of high-throughput water plasma treatment technology in glow-like discharge regime

J Čech^{1,6,*} , P Štáhel¹ , L Prokeš¹ , R Horňák¹ , P Rudolf² , B Maršálek³ , E Maršálová³ , P Lukeš⁴ , A Lavrikova⁵  and Z Machala⁵ 

¹ Department of Plasma Physics and Technology, Faculty of Science, Masaryk University, Kotlářská 2, 611 37 Brno, Czech Republic

² Faculty of Mechanical Engineering, V. Kaplan Department of Fluid Engineering Brno University of Technology, Technická 2896/2, 616 69 Brno, Czech Republic

³ Institute of Botany, Czech Academy of Sciences, Lidická 25/27, 602 00 Brno, Czech Republic

⁴ Institute of Plasma Physics of the Czech Academy of Sciences, U Slovanky 2525/1a, 182 00 Prague 8, Czech Republic

⁵ Division of Environmental Physics, Faculty of Mathematics, Physics and Informatics, Comenius University, Mlynská dolina F1, 842 48 Bratislava, Slovakia

⁶ Department of Physics, Chemistry and Vocational Education, Faculty of Education, Masaryk University, Poříčí 623/7, 603 00 Brno, Czech Republic

E-mail: cech@physics.muni.cz

Received 29 February 2024, revised 24 July 2024

Accepted for publication 23 September 2024

Published 7 November 2024



CrossMark

Abstract

AC discharge in a dense hydrodynamic cavitation cloud in water, called CaviPlasma, has been studied at different discharge parameters. CaviPlasma stands for cavitation and plasma, which are two coupled basic phenomena of the novel technology enabling very high throughput of plasma water processing compared to other current technologies. In this article, the diagnostics and the properties of CaviPlasma discharge are discussed based on optical and electric characterization of the discharge phenomena together with the physico-chemical characterization of the plasma-treated water. The so-called unbridged mode of CaviPlasma operation is described, where the discharge propagates from a metal electrode towards a liquid electrode at the collapsing end of the cavitation cloud. The production of H, O and OH species in the discharge was proven by optical emission spectroscopy. The formation of hydrogen peroxide (H₂O₂) in water was determined by chemical methods. The energy yield for H₂O₂ generation is as high as 9.6 g kWh⁻¹ and the generation rate is up to 2.4 g h⁻¹. The degradation of phenol admixture in water was also studied. The article covers a parametric study enabling the development of tailored applications.

* Author to whom any correspondence should be addressed.

Supplementary material for this article is available [online](#)

Keywords: CaviPlasma, plasma-activated water, hydrodynamic cavitation, electric discharge, hydrogen peroxide, diagnostics, water

1. Introduction

Organic micropollutants of both a biological and chemical nature are a limiting factor for the availability of drinking water. Biological contaminants in the form of pathogenic micro-organisms or chemical residuals in water have to be removed using chemical or physical water treatment methods. While the former is rather efficient, it is prone to the generation of harmful by-products. On the other hand, physical methods do not have this disadvantage, but often suffer from energy and economical inefficiency [1]. Over the last ten years, the authors, together with a multidisciplinary team of researchers, have performed rather extensive research of hydrodynamic cavitation (HC) exploitation for the elimination of cyanobacteria and the characterization of cavitation in various nozzles and orifices [2–6]. They developed several devices for HC generation and concluded that HC alone is not sufficiently powerful and effective in eliminating micropollutants, and that the addition of an advanced oxidation process is required (e.g. the dosage of hydrogen peroxide, ozone, UV irradiation) [7, 8].

Previous research has resulted in a device that inherently combines both methods, named CaviPlasma [9, 10] (erstwhile called Hydrodynamic Cavitation Plasma Jet (HCPJ) in previous papers [11, 12]). In CaviPlasma, the electric discharge within the water vapour cavity generates UV radiation and chemical radicals with oxidative potential. While the first results with cyanobacteria elimination were very promising [11], it is still treated as a black-box, and a thorough understanding of the fluid–plasma interaction is necessary for further utilization and optimization. Here, we note the pioneering work on the utilization of the plasma cavitation phenomenon by Ihara *et al* [13]. They adopted a different geometry of electrodes in the cavitation cloud, where the electrodes were submerged into the cavitation cloud radially downstream of the cavitation cloud.

Applications of plasma technology for water treatment are not new. The generation of reactive oxygen and nitrogen species in liquids (especially water) is now a highly topical field of plasma research [14, 15]. Various liquid discharge technologies have been studied intensively for their cross-disciplinary applications in environmental, bio-medical [16, 17] and agricultural areas [18]. Water and aqueous solutions (media) treated/activated by atmospheric air plasmas—known as plasma-activated water (PAW) or plasma-activated media—were found to have substantial antimicrobial [19] and even anti-tumour properties [20]. In agriculture, exposure to PAW can lead to enhanced seed germination and growth of plants [21] in addition to its strong antibacterial effect [22]. Further

applications of discharge plasmas generated in liquids comprise, e.g. chemical synthesis [23, 24], nanoparticle synthesis [25, 26], destruction of pollutants in waste water [27–31], polymer surface treatment [32], etc.

Nevertheless, the main hindrance remains even after two decades of intensive research efforts towards finding an effective method for large-volume liquid treatment. The direct generation of electrical discharges in liquids is complicated by their generally high breakdown electric field strength ($>1 \text{ MV cm}^{-1}$). In most cases, the initiation of discharge breakdown in a genuine liquid environment is done by applying ultra-fast high-voltage pulses to a highly curved discharge electrode(s) [27, 33]. This limits not only the volume of the generated plasma, but more importantly the power input that can be dissipated into the treated medium. The use of a subsidiary gas-phase environment with the subsequent mixing of plasma-produced species into the liquid is therefore more popular today. The introduction of the gas phase allows a reduction of the breakdown strength to technically more feasible values of 10 kV cm^{-1} . Typical representatives of such an approach are plasma jets submerged in liquid [19], discharges generated above [22, 24] or from the liquid surface [32], discharges in liquid aerosol [15], and discharges produced inside the gas microbubbles introduced [31] or formed inside the liquid volume [28]. Still, until now, none of these methods of discharge plasma generation has been capable of delivering sufficiently high and cost-effective throughput of plasma-treated liquid, as summarized in table 1.

Other important parameters for the comparison of various discharges are the energy yield and generation rate for hydrogen peroxide as the main final product of the discharges under or in contact with pure water; e.g. for the plasma jet to the water surface [22], the generation rate is $71 \mu\text{M min}^{-1}$ and the energy yield is 0.21 g kWh^{-1} . For the spark to the water surface [20], the generation rate is $120 \mu\text{M min}^{-1}$. A detailed overview of these parameters for different discharge types and configurations can be found in the review of Locke and Shih [38]. The main reactions leading to the production and destruction of OH and H_2O_2 can also be found in this review. Detailed kinetic models of reactions in water vapour and in liquid water can be found in [39, 40].

Recently, the joint research team of Masaryk University, Brno University of Technology and the Institute of Botany, Czech Academy of Sciences was able to overcome the technological barrier of delivering sufficiently high and cost-effective liquid throughput by introducing the CaviPlasma technology [9, 10]. Their method employs an energy-efficient generation of a dense hydrodynamic cavitation cloud (HCC), which is

Table 1. Comparison of various underwater discharges. The flow rate means treated liquid flow rate.

Application	Reactor/electrode configuration	Flow rate	Reference
PAW generation	Spark to the water surface	0.7 ml min ⁻¹	[20]
	Plasma jet to the water surface	10 ml min ⁻¹	[22]
	Plasma electrospray	1.7 ml min ⁻¹	[15]
	DBD on or above the water surface immersed Ar+O ₂ or air plasma jets	0.5–25 ml min ⁻¹	[18]
Organic pollution removal (phenols, dyes etc)	Hybrid (corona pulse, water surface DBD)	7 ml min ⁻¹	[27]
	DC diaphragm discharge	38 ml min ⁻¹	[28]
	Wetted wall DBD	0.4–300 ml min ⁻¹	[30]
	DC corona in water; DC diaphragm etc Pulsed DBD	5 ml min ⁻¹	[29]
Cyanobacteria removal	AC discharge in HC (CaviPlasma)	24 000 ml min⁻¹	[11]
Organic dye removal	AC arc in the HC	400 ml min ⁻¹	[13]
<i>E. coli</i> , dye remediation	Discharge in HC	16 700 ml min ⁻¹	[34]
Pharmaceutical removal	Discharge in HC	5 500 ml min ⁻¹	[35–37]

a highly suitable environment for sustaining electrical discharges. The HCC comprises an ample number of tiny voids (cavities) with an internal pressure of liquid vapours of a few kPa only. An advantageous low-pressure environment is formed inside the flowing liquid, where even a moderate high-voltage (HV) field of 1 kV cm⁻¹ can sustain electric discharge in a considerable volume of liquid. The exceptional efficiency of CaviPlasma was demonstrated on cyanobacteria remediation and production of biocidal plasma-treated water [11, 12].

After the CaviPlasma technology public disclosure, the plasma water-treatment technology based on HC generated using high-pressure flow through the set of orifices was reported [34–37]. The authors reported flow rates of 330–1000 l h⁻¹; however, we still lack the detail needed to perform a direct comparison between their system and CaviPlasma technology. From the published data on the system based on high-pressure flow through the orifices [34–37], we have estimated the hydrogen peroxide energy yield to be about three times lower than the maximum yield of CaviPlasma technology presented in this paper. In addition, the flow rate reported on that system was from 20% to 70% of that achieved using CaviPlasma technology ([11] and data reported in this paper).

The present paper focuses on the explanation and diagnostics of the CaviPlasma technology used in these experiments. The discharge was analyzed using a high-speed camera and intensified (gated) CCD camera (ICCD camera). The electrical characteristics of the discharge were measured using digital storage oscilloscopes with HV probes and current monitors. Optical emission spectra were recorded in order to identify the emitting particles in the discharge. The OH radical is the dominant oxidant in the discharges in water. The OH concentration in the liquid water was determined *in situ* from the OH reaction with terephthalic acid (TA) added to water. Molecular hydrogen and hydrogen peroxide are the main stable products of the discharge in water. Hydrogen peroxide is formed via the recombination of two OH radicals, and its concentration was determined by two independent methods. The H₂O₂ production efficiency was studied for changing

discharge parameters—the input power, the pressure above the water surface at the outlet (back-pressure) and the water flow rate. The efficiency of CaviPlasma for waste water remediation was tested on phenol removal from water. The phenol removal in the discharge in water is mainly due to the phenol reaction with OH radicals, which points out the importance of OH radicals in plasma technologies. Phenol removal from water was already reported by authors to test their plasma technology for waste water remediation; see [30].

2. Experimental setup

2.1. Plasma source

The configuration of the CaviPlasma device is illustrated in figure 1. Generally, the diagnostic setup of the presented CaviPlasma unit is based on the setup of HCPJ published in [12], which was adapted to enable phase-resolved optical imaging, optical emission spectroscopy and electric measurements on the discharge in HCC, as well as the continuous monitoring of the water flow rate at the hydraulic pump outlet. Figure 1 shows the setup and the visualization of the discharge ignited in the reaction chamber.

The setup of the CaviPlasma unit diagnostics consists of three parts: (i) a hydraulic circuit with the flow meter and the vacuum system with pressure gauge; (ii) an electrical circuit consisting of electrodes, HV power supply and oscilloscopes with current and voltage probes; and (iii) optical diagnostics consisting of an ICCD camera, high-speed video camera and optical emission spectrometer.

The hydraulic system consists of a reaction chamber made of a transparent polycarbonate tube (28 cm long, 12 mm outer diameter and 10 mm inner diameter), allowing for optical diagnostics of the discharge in the HCC. The cavitation was induced in the reaction chamber using a fast-flowing liquid through a convergent–divergent nozzle (Venturi nozzle). The nozzle throat had a minimum inner diameter of 3.5 mm. The water stream through the Venturi nozzle was maintained using

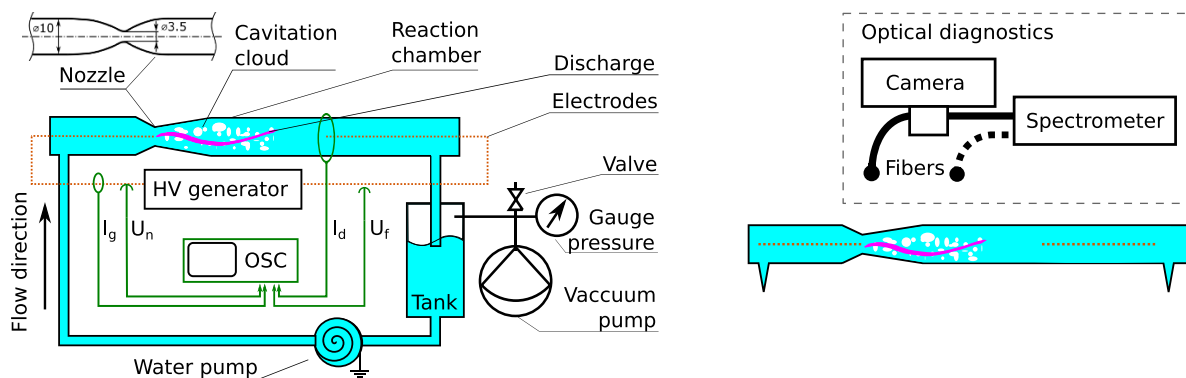


Figure 1. Experimental setup: (left) Hydraulic and electric circuit with electric probing; (right) Setup of optical diagnostics with respect to the discharge tube.

a CALPEDA CTM61/A hydraulic pump (Calpeda S.p.A., Montorso Vicentino, Italy) rated at 330 W power input driven using a VYBO A550Plus variable frequency driver. There is a certain parametric window within which the required water flow rate and the HCC length can be set using combined control of the hydraulic pump driving frequency and back-pressure at the water reservoir maintaining a pressure difference in the reaction chamber. The required back-pressure at the water reservoir was regulated using a vacuum system consisting of a single-stage membrane vacuum pump VM 40 D (LAVAT, Czech Republic) evacuating the water tank, needle-valve regulator and a gas pressure gauge Leybold Heraeus no. 160 40 (Leybold Heraeus, Hanau, Germany).

The whole hydraulic circuit was connected using 1" connection hoses made of PVC. A Georg Fischer GF 355 DN 32 PVC/EPDM no. 199.335.003 analogue variable area flowmeter (Georg Fischer, Schaffhausen, Switzerland) was inserted directly at the hydraulic pump vertical outlet to monitor the water flow rate. For UV sensitive diagnostics of the discharge emission a reaction chamber made of poly-methyl methacrylate (PMMA) tube was used instead.

The discharge in the HCC was generated using an alternating high voltage imposed on the two cylindrical electrodes, illustrated as a dashed orange line in figure 1. These electrodes were positioned coaxially within the liquid stream. The first electrode was positioned in the convergent part of the nozzle 4 mm before the throat minimum diameter (nozzle electrode). The opposite electrode (flow electrode) was placed 15.5 cm away from the nozzle electrode downstream of the reaction chamber, i.e. in the liquid phase beyond the HCC collapse region. The electrodes were made of copper wire of 2 mm diameter, 4 mm in diameter including insulation, which was stripped of the flow electrode at a length of 7 mm. The nozzle electrode was cut straight, i.e. only the tip of the electrode was exposed.

A custom-made tunable HV generator was employed to energize the discharge. This generator consisted of a low-voltage, high-frequency tunable generator with adjustable output voltage amplitude and a high-voltage transformer for up-conversion to HV. The HV generator generated a sine wave waveform at a frequency range of 30–70 kHz and a voltage

amplitude up to 20 kV. The total average input power of the HV generator was measured using an ORBIT MERRET OM 402PWR network analyzer (ORBIT MERRET, Prague, Czech Republic)

The diagnostic setup consisted of optical diagnostics (imaging and spectroscopy), electrical diagnostics (current and voltage measurements) and treated water diagnostics (H_2O_2 measurement, pH, conductivity and temperature measurements). The diagnostic setup and methods are given in detail in the following section.

2.2. Discharge and product diagnostics

The electrical diagnostics consisted of the measurement of high voltage on the electrodes and current flowing through the reaction chamber. For the current and voltage acquisition, two models of four-channel digital storage oscilloscopes were used: (i) the LeCroy WaveRunner 6100A (LeCroy Corporation, Chestnut Ridge, NY, USA) with a bandwidth of 1 GHz, a sampling frequency of 5 GSa s^{-1} and an 8-bit AD converter; (ii) Keysight Infinium DSO-S 204A (Keysight Technologies Inc. Santa Rosa, CA, USA) with a bandwidth of 2 GHz, a sampling frequency of 20 GSa s^{-1} and a 10-bit AD converter. The currents were measured using Pearson 6585 and Pearson 2877 current monitors. The Pearson 6585 current monitor inner diameter of 2 in enabled direct sensing of the current flowing through the reaction chamber (i.e. the sum of the currents flowing through the discharge and the HCC). The electrode HV potentials were monitored using Tektronix P6015A HV probes (1:1000).

Visualization of the CaviPlasma dynamics was performed using a high-speed digital camera and phase-resolved imaging using the ICCD camera. The Sony CyberShot DSC-RX10 III camera (Sony Corporation, Tokyo, Japan) was employed to monitor the evolution of the plasma cavitation phenomenon dynamics in real time. The CyberShot camera ($24\text{--}600\text{ mm} / f\ 2.4\text{--}4$) enabled high-frame-speed capture at a frame rate of 1000 fps at a reduced effective resolution of 1136×384 pixels across three colour channels (red, green and blue). The dynamics of the discharge cavitation phenomenon could be followed with a temporal resolution of 1 ms

averaging approximately 60 discharge periods within a single frame. The estimated maximum spatial resolution achieved was 0.25 mm in the lateral dimension and 0.4 mm in the radial dimension.

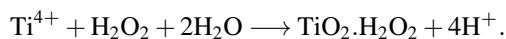
For highly temporally resolved imaging, the ICCD camera PI-MAX3-1024i-SR-46-CM from Princeton Instruments was used (Princeton Instruments, NJ, USA). The ICCD camera enables phase-resolved imaging of the discharge with a spatial resolution of 1024×1024 pixels and temporal resolution down to 2.8 ns (the minimum timeframe used was 100 ns due to low discharge emission). For the capture, the ICCD camera could be mounted with a SIGMA 105 mm 1 : 2.8 EX DG MACRO lens (SIGMA Corporation, Kanagawa, Japan), or for UV sensitive imaging with a CoastalOpt 105 mm $f/4$ UV-MICRO-APO lens (Jenoptik AG, Jena, Germany). The ICCD camera photocathode gating was synchronized to the HV generator voltage output to achieve phase-resolved imaging of the discharge.

Optical emission spectra of the discharge were sequentially recorded in two spectral ranges (UV and UV–VIS–NIR). The discharge emission was captured from two distinct regions sensing the discharge emission just beyond the nozzle electrode and the region of the HCC 80 mm downstream in the direction of the cavitation cloud flow towards the flow electrode. A pair of UV transparent quartz optical fibres (2 m in length, with a single fibre diameter of $400 \mu\text{m}$ (Avantes BV, Apeldoorn, The Netherlands) was adopted. The fibres were positioned 12 cm above the discharge tube and the sampling spots for spectra acquisition had approximately 10 mm radius due to the acceptance angle of the fibres. The spectra were captured without temporal resolution using two fixed grating AvaSpec ULS3648TEC-USB2 spectrometers (Avantes BV).

The spectral range of the survey spectrometer spanned from 200 nm to 1100 nm and it was equipped with a UA grating (200–1100 nm) and a $25 \mu\text{m}$ wide entrance slit. Order-sorting coatings with 350 nm and 600 nm long pass filters were employed to suppress overlapping spectral orders. The theoretical resolution achieved by this survey spectrometer configuration was approximately 1.1 nm. In order to acquire discharge emission in the UV range with higher spectral resolution, a second spectrometer was utilized. This spectrometer, equipped with a UE grating (290–395 nm) and a $10 \mu\text{m}$ wide entrance slit, offered a theoretical spectral resolution on the order of 0.1 nm. The recorded spectra were subsequently analyzed using Spectrum Analyzer 1.8 (Masaryk University, Brno, Czech Republic, [41]) and massiveOES (Masaryk University, Brno, Czech Republic, [42, 43]).

The measurement of hydrogen peroxide concentration was conducted using Quantofix peroxide test strips with ranges of $0\text{--}100 \text{ mg l}^{-1}$ and $0\text{--}25 \text{ mg l}^{-1}$. The concentration of H_2O_2 was evaluated using the test strip reader, the Quantofix Relax reflectometer (MACHEREY-NAGEL, Dueren, Germany). The reader provides readings with an accuracy of 20%. This method enables fast semi-quantitative

measurement of a large quantity of samples. For the reference measurements, the colorimetric method was employed based on the chemical reaction of H_2O_2 with titanium sulphate reagent. This reaction is usually written as



The pertitanic acid $\text{TiO}_2 \cdot \text{H}_2\text{O}_2$ (H_2TiO_4) formed exhibits a yellow colour, and its concentration can be quantified using UV–VIS absorption spectroscopy to determine the hydrogen peroxide concentration [44].

The OH concentration in liquid water was measured *in situ* by the following procedure. OH converts TA to fluorescent 2-hydroxyterephthalic acid (HTA). The HTA concentration was determined using fluorescence spectrometer Shimadzu RF-6000. The HTA was excited by UV light (wavelength 310 nm) and the HTA fluorescence peak was detected with a maximum intensity of 425 nm. The area of the fluorescence peak was measured and the HTA concentrations were calculated based on the calibration curve. The pH and conductivity were monitored. The total treated volume of the TA solution was 2.5 l; the initial TA concentration was 2 mM stabilized by 5 mM NaOH.

The phenol degradation in CaviPlasma was also studied. For this experiment, a solution of $500 \mu\text{M}$ of phenol and 7 mM of NaH_2PO_4 in 2.5 l of deionized water was prepared. The concentrations of phenol and its degradation by-products were measured using the high-performance liquid chromatography (HPLC) system Shimadzu LC-10Avp with UV and fluorescence detection. The identification and quantitative analysis of by-products were based on peak retention times, ultraviolet absorption spectra, and calibration with standards obtained commercially (Sigma-Aldrich). Hydroquinone, catechol, 1,4-benzoquinone and hydroxy-1,4-benzoquinone were detected simultaneously with phenol. Analyses were made using a $5 \mu\text{m}$ reversed-phase Supelcosil LC-18 column ($25 \text{ cm} \times 2.4 \text{ mm}$; Supelco). An isocratic method with a solvent mixture of 10% acetonitrile and 0.5% acetic acid in deionized water was used as the eluent with a flow rate of 0.4 ml min^{-1} . UV detection was performed at 250, 274 and 290 nm. Fluorescence detection was done with excitation and emission wavelengths of 271 nm and 297 nm, respectively. The detection limit for the HPLC analysis was $0.01\text{--}0.1 \mu\text{mol l}^{-1}$ (depending on the compound and the detection used).

Temperature measurements were conducted using a Greisinger GTH 175 Pt1000 thermometer (Senseca Germany, Regenstauf, Germany) with a range from -199°C to $+199^\circ\text{C}$. Electrical conductivity was measured using a Mettler Toledo Conductivity FP30 (Mettler Toledo, Greifensee, Switzerland) with Mettler Toledo LE740 (range: $0.01\text{--}500 \mu\text{S cm}^{-1}$) and LE703 (range: $0.01\text{--}200 \text{ mS cm}^{-1}$) probes. The pH values were determined using the Mettler Toledo FP20 pH meter with LE420 probe (range: $0\text{--}14 \text{ pH}$).

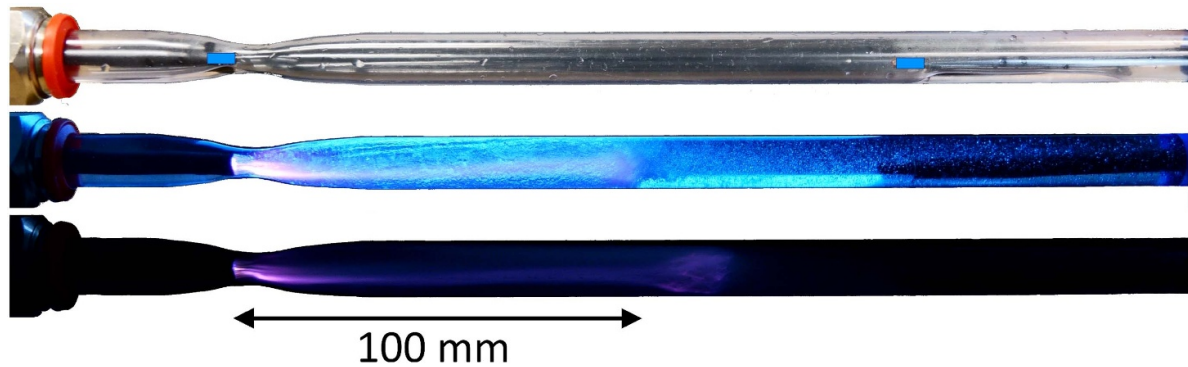


Figure 2. The visual appearance of CaviPlasma: (top) empty discharge tube with position of electrodes (blue bars); (middle) discharge with flash-enhanced HCC at 1/20 s exposure; (bottom) discharge at 10 ms exposure. The water flow direction is from the left to the right.

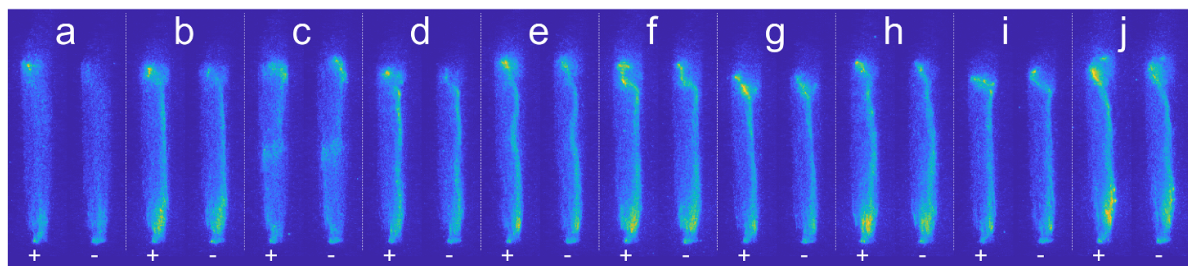


Figure 3. Visual appearance of single half-periods of discharge taken using an ICCD camera. Images labelled (a) to (j) represent pairs of consecutive half-periods of discharge with respect to the polarity of nozzle electrode (labelled + and -). The orientation of the discharge tube in images is vertical, i.e. rotated 90 degrees anti-clockwise compared to figure 2. The water flow is directed upwards. The position of the nozzle electrode is at the bottom. The flow rate was $1.2 \text{ m}^3 \text{ h}^{-1}$.

3. Experimental results

3.1. Visual characteristics

Images of the CaviPlasma device are shown in figure 2. The top picture shows the discharge tube with the convergent-divergent Venturi nozzle without water. The position of the electrodes is marked by the blue colour. The distance between the electrodes was 15.5 cm. The middle picture shows the CaviPlasma in operation; the back-fill flash was used for visualization of the HCC and the flow downstream of the HCC/plasma zone. The bottom image shows the discharge in the HCC taken with a short exposure time. The discharge was generated by an applied HV of 6.4 kV with a frequency of 65 kHz; the applied power was 0.4 kW. The value of the applied power given here and also later in this paper was measured by an Orbit Merret OM 402PWR network analyzer and represents the total input power of the HV generator from the grid. Tap water with a conductivity of 0.5 mS cm^{-1} was used for this measurement; the water flow rate was $1.2 \text{ m}^3 \text{ h}^{-1}$ and the back-pressure was 40 kPa.

Cavitation is the formation of vapour bubbles (more correctly, ‘voids’) within a liquid in low-pressure regions that occurs in places where the liquid has high velocity. The HC phenomenon occurs due to Bernoulli’s principle. The cavities (vapour voids) form when the pressure of the liquid has been reduced to its vapour pressure; they expand as the pressure is further reduced along with the flow, and suddenly collapse

when they reach regions of higher pressure. These cavities were saturated with liquid vapours at pressures of several kPa (depending on the water temperature; e.g. for a temperature 20°C it is 2340 Pa), creating favourable conditions for the generation of the cavity plasma discharge phenomenon. A reduction in back-pressure facilitated a substantial expansion of the cavitation cloud region, resulting in a prolonged active plasma zone.

The discharge was further visualized using an ICCD camera; see figure 3. In this figure, 10 non-consecutive periods of discharge are shown, labelled (a) to (j). Each period was captured in both consecutive half-periods, marked as positive and negative with respect to the polarity of the nozzle electrode in contact with the discharge. The images are rotated 90 degrees anti-clockwise with respect to the orientation of the photographs in figure 2. The visual appearance and the discharge path depend on the actual state of the HCC. In periods (a) and (c) the discharge column is hardly visible. This situation is most probably caused by the fact that the discharge column is overclouded by the HCC along the line of sight. In part (c) there is also a visible HCC disturbance; see below for details.

The discharge column has three regions: (i) the nozzle electrode attachment zone, with a high-velocity divergent stream of water passing through the divergent part of the nozzle. There the lowest pressure and several streams of cavities are generated at the edge of the electrode. Then, the narrow discharge column is visible (ii), bridging the HCC towards the end of the

cavitation zone. The shape of the column in the HCC depends on the actual state of the HCC. Our simulations reveal that the on-axis and the outer part of the HCC (radially) are probably the areas with the lowest stream density, i.e. the areas with the highest density of cavities; see supplementary material figure S1. As the discharge is generated in the gas phase, the discharge path follows the vapour-rich regions of the HCC. The results of the HCC simulation and experimental observation of the discharge channel from the high-speed cameras suggest that the discharge burns in the consecutive gas phase of the HCC (so-called supercavitation) spanning from the nozzle electrode to the end of the HCC. At the end of the HCC (iii) the collapse of the cavitation occurs, forming a highly turbulent HCC plug. Here, the discharge faces the collapse of the gaseous phase and is visually branched into luminous filaments, resembling the streamer branching in high-pressure discharges.

It can be seen that the discharge emission is more intense in the area of negative polarity of the electrode (cathode region); see ICCD images in figure 3. In the case of a metal nozzle electrode, a thin luminous layer or spot at the edge of the cathode is observed, followed by a less luminous thin layer and a discharge column in the HCC. Considering the rather high voltage and low currents recorded in e.g. figure 7, we can assume that the observed discharge is probably a glow or abnormal glow discharge. We also observe more intense emission from the HCC plug region during the ‘liquid’ cathode phase; however, we could not identify the same structure as in the nozzle (metal electrode) region in the cathode phase. This could be the result of the complex HCC structure in this region or the different mechanisms. The visual appearance of the cathode phase in the HCC plug resembles streamer-like branched channels. However, the phase-resolved ICCD imaging shows that mostly a single luminous channel per period is visible at the end of the discharge/HCC channel. From this we can conclude that the discharge probably follows only one branch of the luminous structure per period. The observed branching is then the effect of the highly dynamic behaviour of the collapsing HCC, where the discharge follows the pre-ionized path and then hops through different channels in the HCC plug, whichever is more favourable at the moment.

3.2. Cavitation cloud characteristics and the role of the cavitation cloud parameters on discharge generation

The behaviour of the cavitation cloud (state of the cavitating flow) is influenced by the experimental conditions [4]. The cavitating flows can be assessed based on the pressure and the energy (velocity) applied to the water stream flowing through the Venturi tube (in so-called cavitation number)[4]. From the point of view of the electric discharge generation and discharge dynamics, there are three important regions of the HCC (see images in figure 2).

The onset of HCC takes place at the tip of the nozzle electrode. The cavitation cloud in the form of several cavitation streams can be located here (see figure 2). A gaseous low-pressure environment is created there due to the decrease in

the hydrodynamic pressure below the saturated water vapour pressure. This pressure dependency can be approximated by the IAPWS formula [45], and under room temperature conditions (20 °C) the pressure in the cavitation is 2340 Pa. After the nozzle the cavitation cloud expands, forming a highly dynamic liquid–gas mixture, which is typical of cavitating flows. The pure HC has a negligible effect on the heating of the liquid. While extremely high temperatures have been reported for collapsing cavitation bubbles [46, 47], the total amount of heat produced by these bubbles is very small. Experiments with mechanically induced growth and collapse of a single bubble in water found that a temperature decrease of 3 °C during bubble growth and a temperature increase of 4 °C during bubble collapse occurred, as observed by infrared camera [48]. Most of the temperature increase in pure HC experiments is attributed to the water pump. In the case of a closed hydraulic loop, all pump energy is dissipated into heat. Also, very small concentrations of hydrogen peroxide ($\sim 10^{-12}$ mol l⁻¹) are generated by HC itself [49]. Our upper limit estimation of these concentrations from experiments with cavitation itself is 0.7 mg l⁻¹.

When a high electric field is applied to the HCC, an electric discharge can be ignited in the HCC and the discharge creates its path through the cloud there. The HCC has to develop effectively into a high resistivity volume between the electrodes to ensure the development of high reduced electric field space in the gaseous environment necessary for the discharge onset. The breakdown reduced electric field for water vapour is reported to be 190 Td [50]. Then, the calculated breakdown voltage for our conditions is 2.2 kV and 12.1 kV for HCCs with a length of 2 cm and 11 cm, respectively. The discharge current is stabilized by the high resistivity of the water column between the HCC end and the flow electrode. The exact path of the discharge through the HCC is of stochastic nature. The HCC is subject to variations in its length and the occurrence of hydrodynamic shocks in the stream propagating along the tube (indeed, the flow is locally supersonic and shock waves are transmitted through the liquid–vapour mixture).

The discharge propagation in the dynamic conditions of the HCC is illustrated in figure 4. In this figure, the development of the HCC, and respectively the discharge, is followed using fast camera imaging. The HCC represents a naturally stochastic system, where disturbances in the liquid flowing through the nozzle lead to disturbances in the cavitation cloud. The discharge then follows the HCC shape, resulting in the bending or breaking of the path of the discharge. The propagation of such an event is denoted by the arrow in figure 4. The propagation time scale of the disturbance is of the order of milliseconds, which is approximately two orders of magnitude longer than the discharge event time scale. The estimated propagation velocity of the disturbance shown in figure 4 was 9.6 m s⁻¹ at a flow rate of 1.2 m³ h⁻¹.

3.3. Discharge characterization

In this subsection, the results of the studied influence of the back-pressure on the HCC length, and electrical and optical parameters of CaviPlasma will be given.

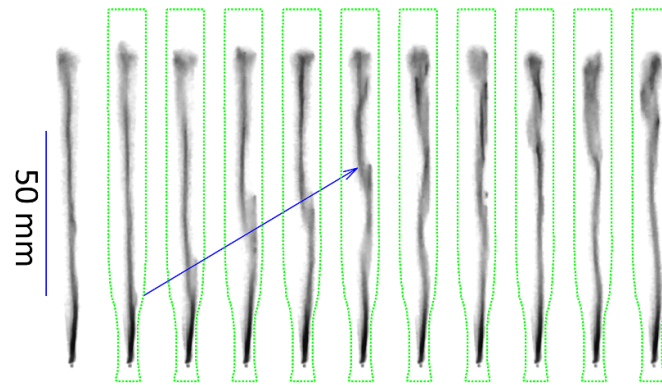


Figure 4. Consecutive frames of the high-speed video capture of discharge influenced by HCC disorder acquired at 1000 fps with exposure time 1 ms representing about 65 periods of the discharge. Starting from the second frame one can follow the disturbance propagating along the tube. The orientation of the discharge tube on images is vertical, i.e. rotated 90° anti-clockwise compared to figure 2. The water flow is directed upwards. The position of the nozzle electrode is at the bottom end of the discharge channel (in grey tones). The flow rate was $1.2 \text{ m}^3 \text{ h}^{-1}$.

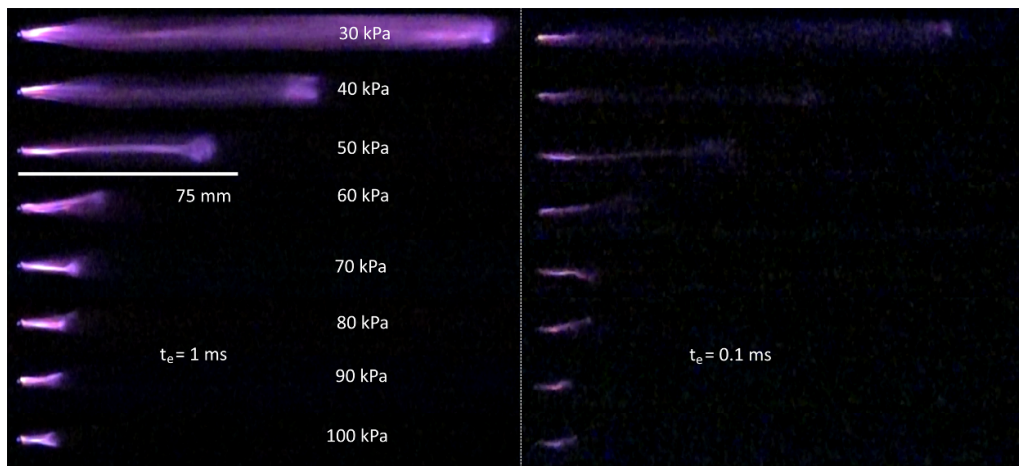


Figure 5. Influence of back-pressure on the cavitation cloud and plasma channel—visual appearance at different exposure times. The orientation of images is the same as in figure 2, and the water flows from left to right. The nozzle electrode tip is at the left edge of the luminous channel. The flow rate was $1.2 \text{ m}^3 \text{ h}^{-1}$.

3.3.1. Influence of the back-pressure on the cavitation cloud and plasma parameters. In order to explore the parameters of the CaviPlasma for an extended length of HCC without manipulating with the water stream flow rate, we have to induce a pressure drop at the outflow of the discharge tube. This was performed by decreasing the back-pressure at the water reservoir using the vacuum pumping system. The influence of the back-pressure on the HCC length and discharge channel, respectively, was measured for tap water. The images of the CaviPlasma for different back-pressures are shown in figure 5 for two exposure times. The water flow rate was $1.2 \text{ m}^3 \text{ h}^{-1}$ and the applied power was 0.5 kW at a frequency of 63 kHz. The HCC length, and respectively the discharge channel length, was determined from the discharge emission in the HCC.

A high-speed camera was used to capture 2000 consecutive frames at 1000 fps for each back-pressure condition. The axial profile of emission intensities of each frame was obtained by summation in the radial direction. The resulting maps are shown in the Supplementary material in figure S2. The length

of the discharge channel was determined from these maps for each frame of the capture and then statistically processed, resulting in boxplot visualization, using Matlab; see figure 6. The dependence shown in figure 6 can be fitted by the formula $l = a/p^b$, where l is the plasma channel length in units of mm and p is the back-pressure in units of kPa, resulting in numerical values of the parameters of $a = (1.82 \pm 0.06) \times 10^5$ and $b = 2.08 \pm 0.01$.

The current–voltage waveforms of discharges generated in tap water for two HCC lengths are shown in figure 7. The reduction of the back-pressure induces prolongation of the HCC and correspondingly the discharge channel; see figure 5. This results in a change of the electrical parameters of the discharge cavitation system.

In figure 8, the evolution of the current–voltage characteristics is shown for the discharges generated in tap water with respect to the back-pressure reduced from the atmospheric pressure down to 30 kPa. The total applied power was kept constant at 0.5 kW; however, the voltage and current amplitudes vary with the variation of the length of the HCC and

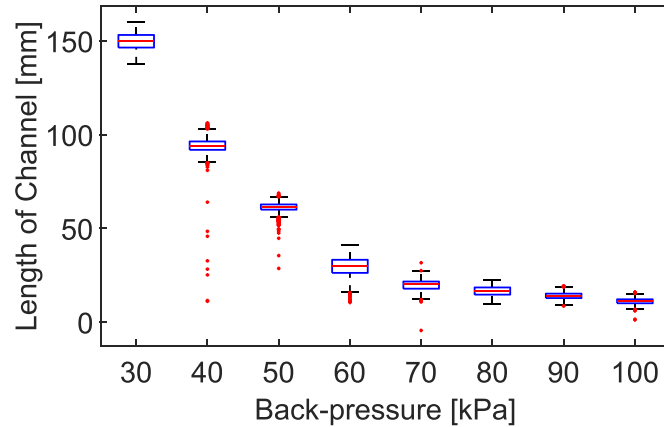


Figure 6. Influence of back-pressure on the cavitation cloud, resp. the plasma channel length. The red lines represent median values, the boxes represent interquartile ranges, the black lines represent non-outlier maxima and minima, and the red dots are outliers. The flow rate was $1.2 \text{ m}^3 \text{ h}^{-1}$.

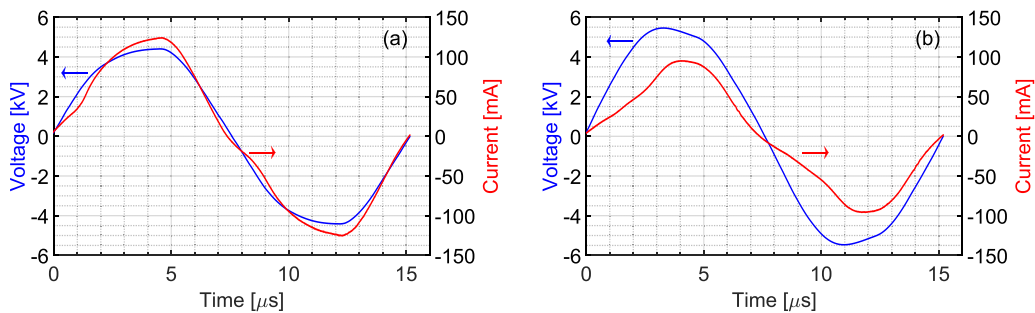


Figure 7. Comparison of current–voltage waveforms for (a) 2 cm and (b) 11 cm long HCC. The discharges were generated in tap water. The total power input of HV power generator was kept at 0.5 kW. The blue lines show the voltage between the electrodes, the red lines show the total current flowing through the discharge tube. The flow rate was $1.2 \text{ m}^3 \text{ h}^{-1}$ and the back-pressure was 100 kPa for 2 cm HCC length and 40 kPa for 11 cm HCC length, respectively.

discharge channel, respectively (see figure 7). For easier comparison, the current–voltage characteristics in figure 8 are normalized to the respective peak values of the HV.

Within the discharge period we could identify three regions on the current–voltage characteristics; these discharge phases can be compared using the phase-resolved discharge images in section 3.3.3. The temporal evolution of the current and voltage represents the anti-clockwise motion of the points on the current–voltage characteristics.

In the first phase, when the voltage is rising from the zero value, the slopes of the characteristics are quite similar regardless of the back-pressure, i.e. the HCC length. This indicates that in this phase, before the voltage exceeds a certain threshold value, the conductivity of the system is relatively low and does not vary significantly with the back-pressure (HCC length).

Then, as the voltage value keeps rising, the discharge is intercepted, resulting in a decrease in the slope, which indicates an increase in the conductivity of the discharge cavitation system. After the peak voltage value is achieved (the right-most point on the graph), the voltage starts to decline; however, the slope of the plot remains small, indicating the high conductivity of the system (more pronounced for a shorter HCC at larger back-pressures).

A further decrease in the voltage again results in a change of the slope of the characteristics. The slope is higher and rises with the time, indicating a gradual decrease in the conductivity of the system related to the discharge decay.

When the voltage polarity changes, the situation is repeated for the negative polarity of the discharge. The characteristics at low applied voltage, i.e. near the polarity reversal points, exhibit current oscillations. As these oscillations occur before the inception voltage is reached (or after the discharge collapse), we suspect the HV generator solid-state amplifier polarity reversal to be the cause of this behaviour.

Let us analyze the described behaviour in more detail. A longer HCC means a shorter water column between the HCC plug and the flow electrode. This water column works as an effective liquid ballast resistor limiting the discharge current. A longer HCC therefore results in a lower liquid ballast resistor resistance. However, we did not observe significant changes in the current–voltage plot slope (i.e. the resistance) in the phase before the discharge onset. This indicates that there is another resistance in series with relatively higher magnitude than the ballast resistance of the water column. This high-resistance region should be the HCC itself, which is composed of a gas–liquid mixture; see figures 2 and S1.

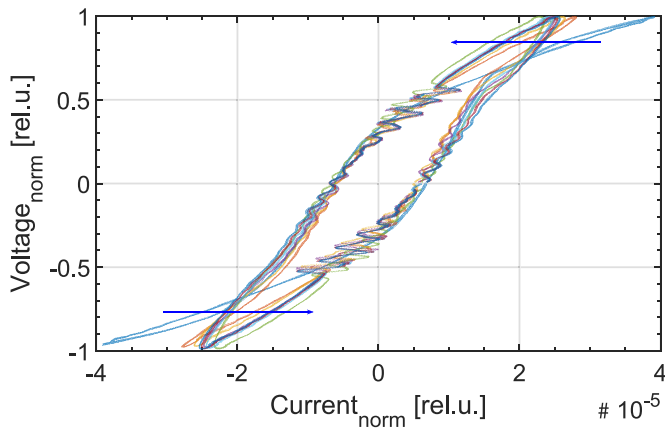


Figure 8. Current vs. voltage plots of discharge in operation with respect to back-pressure. For comparison, the voltage waveforms were normalized to unity maxima and current waveforms were normalized accordingly to maintain the current-to-voltage ratios. The arrow direction indicates the evolution with respect to the increasing back-pressure from 30 kPa to 100 kPa. The water flow rate was $1.2 \text{ m}^3 \text{ h}^{-1}$, and the applied power was 0.5 kW at a frequency of 63 kHz.

If we follow the effective impedance of the system during the discharge phase by means of current–voltage plots in figure 8, we can see that the lowest slope (i.e. highest conductivity) is achieved for a back-pressure of 30 kPa. Under these conditions, the HCC and thus also the discharge start to bridge the distance between both electrodes, leading to a transition from the liquid electrode to the metal electrode regime. When the back-pressure rises, the HCC/discharge shortens, resulting in the ballast water column prolongation and an increase in its resistance. This limits the discharge current and leads to a reduction in the discharge conductivity, resulting in a greater slope of current–voltage characteristics during the discharge phase. In the active discharge phase, the resistance of the HCC region and the HCC plug will have a limited effect because the discharge is effectively short-circuiting this turbulent liquid–vapour region.

3.3.2. Optical emission spectra under different back-pressures. The experimental conditions were the same as in section 3.3.1. The optical emission spectra of the discharge generated in the HCC were taken according to section 2.2. The spectra were temporally unresolved with an integration time of tens of thousands of discharge periods and higher. The spectra were corrected to the sensitivity of the respective quartz fibre and spectrometer setup and the attenuation of the wall of the PMMA discharge tube. The influence of the absorption of the water column was also considered.

The model of the water column of 5 mm was taken as the average worst case scenario for radiation transport from the centre of the non-cavitating water column. From the data in the literature [51–54], the signal attenuation due to the water column was estimated in the measured spectral range. For OH emission in the UV range, the estimated absorption is well below 0.1%. The intensity drop is below 0.5% in the range

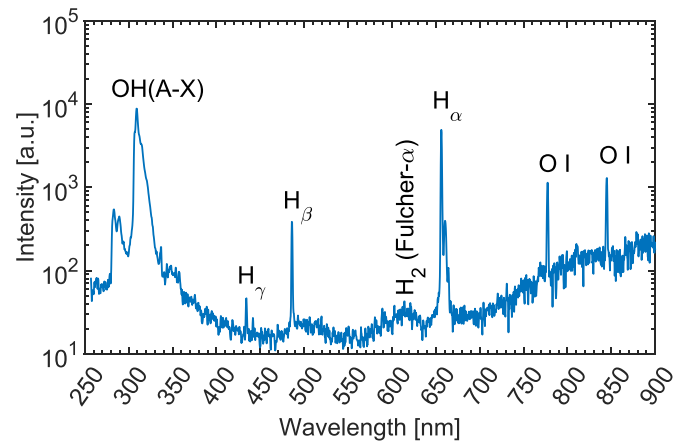


Figure 9. Optical emission spectrum of the CaviPlasma discharge at back-pressure of 100 kPa for tap water flow rate of $1.2 \text{ m}^3 \text{ h}^{-1}$. The applied power was 0.5 kW. The integration time was 1.5 s (normalised to 1 s). The emission is recorded above the discharge channel next to the nozzle electrode.

of 300–700 nm, around 1.2% at 777 nm (O triplet), and rises to about 3.5% of the original intensity in the NIR range up to 900 nm. Therefore, we did not include this correction in the presented spectra and the spectra used for OH rotational temperature measurement.

The reflections and refractions in the cavities represent a completely different problem. Without a solid numerical model, which is beyond the scope of this publication, the escape factor of the light emission in a particular direction cannot be determined. The presented spectra are therefore uncorrected to this effect. From the flat and very low absorption coefficient of water at a wavelength of 310 nm, we can assume that the OH band intensity-based calculations will not be highly affected by the aforementioned processes. However, the relative intensity comparison between OH, H_α and O triplets could potentially be affected by these processes.

The presented spectra were taken under conditions optimizing the signal-to-noise ratio. The integration time was set at each discharge condition separately to achieve high separation of the signal from the noise floor. The integration times for survey spectra span from 1.5 s to 10 s. The integration times for the higher resolved UV spectra span from 10 s to 45 s. The presented spectra were normalized to an integration time of 1 s.

In the spectra from the nozzle region, the H_α , H_β and H_γ lines from the Balmer series were identified together with the emission lines from oxygen triplets (OI 777 nm and 844 nm) and strong emission of the OH radical (OH(A-X)); see figure 9.

We also detected the continuum in the UV part of the spectra, most probably the H_2 one. There is also a sign of another NIR continuum. This could be due to thermal emission; however, an NIR/IR spectrometer would be necessary to confirm this hypothesis. We also identified a H_γ line (a faint emission though) and a low emission of molecular nitrogen second positive system (N_2 SPS) in the spectra of the CaviPlasma

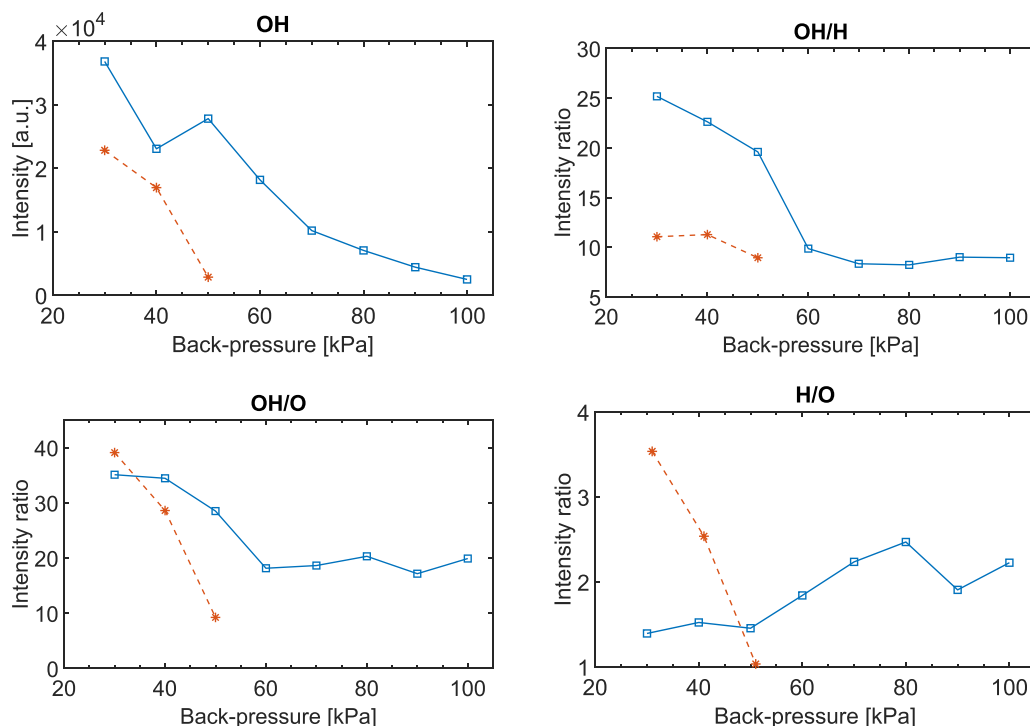


Figure 10. Dependence of spectral characteristics on the back-pressure. The intensities and ratios of intensities were given for OH (A-X) band, hydrogen lines (Balmer series) and oxygen triplets, respectively. The blue lines show the intensities and their ratios at the nozzle position ('Nozzle'), and the red lines at a distance 80 mm from the nozzle ('Flow'). The integration times span from 1.5 s to 10 s. The presented spectra were normalized to an integration time of 1 s. The water flow rate was $1.2 \text{ m}^3 \text{ h}^{-1}$ and the applied power was 0.5 kW.

emission downstream of the discharge channel near the liquid electrode.

The integrated intensities of the emission of the OH radical, atomic hydrogen and oxygen were calculated from the spectra as well as selected ratios of them, and the results are given in figure 10. With the increase of the back-pressure, the overall intensity of the optical emission decreases and the ratio of the spectrum constituents changes. Let us analyze the emission from the nozzle region first.

At the nozzle position, we see that the emission intensity of the OH radicals with respect to the oxygen and hydrogen atomic emission is higher for lower back-pressure, representing a longer HCC and thus a longer discharge channel. The H/O ratio slightly increases with the increasing back-pressure. Based on the emission ratios, we can divide the discharge conditions into two groups:

- (i) For a back-pressure below 60 kPa (i.e. HCC length above 30 mm) the OH/H and OH/O ratios increased with the prolongation of HCC (lower back-pressure);
- (ii) For a back-pressure above 60 kPa (i.e. HCC length below 30 mm) the OH/H and OH/O ratios were the lowest, and they were not influenced by the back-pressure changes. This plateau corresponds to a shorter HCC length, i.e. to conditions where the HCC length is much less sensitive to the back-pressure value; see figure 6.

At the downstream position, at a distance of 80 mm from the nozzle (marked as 'Flow'), the OH intensity and intensity

ratios for OH, O and H decrease in all cases when the back-pressure increases. The relative intensities of hydrogen lines to oxygen lines and hydrogen lines to OH emission were approximately two times higher than those above the nozzle region, indicating differences in plasma processes in the nozzle and channel regions, respectively; see figure 10.

At a back-pressure of 50 kPa, the HCC length was slightly shorter than 80 mm; however, a very weak spectrum was obtained for the downstream position of the fibre. The radius of the collecting spot was approx. 10 mm and the HCC length naturally fluctuates in the same order of magnitude and on a time scale shorter than the integration time; see figure 6 and figure S2 in the supplementary material. The measured spectra in the downstream position at 30 kPa back-pressure represent the emission of the discharge channel, while for 50 kPa back-pressure the emission is collected from the area of the collapsing end of the HCC. For back-pressures higher than 50 kPa, the HCC (discharge) length was too short for the spectra to be obtained at this position above the discharge tube.

The rotational and vibrational temperatures of OH(A-X) were obtained using massiveOES software [42, 43] from the OH spectra taken using the higher resolved UV range spectrometer described in section 2.2; see figure S3 in the Supplementary material. The integration times span from 10 s to 45 s. The obtained temperatures are shown in figure 11. When the OH(A-X) spectra were processed using massiveOES software, the distributions of the rotational and vibrational excited states of the OH radical could be obtained using a state-by-state simulation. According to the literature [42,

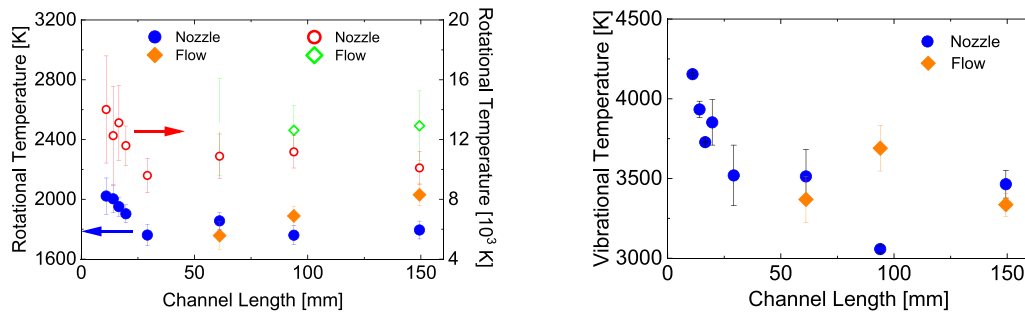


Figure 11. Dependence of rotational temperatures (left) and vibrational temperature (right) on HCC channel length derived using massiveOES software from OH (A-X) spectra. The ‘low’ rotational temperature—full symbols and left axis; the ‘high’ rotational temperature—open symbols and right axis. The circles (full and open) mark the values measured at nozzle position (‘Nozzle’), the diamonds (full and open) mark the values measured at downstream position (‘Flow’). The integration times for the OH spectra span from 10 s to 45 s. The water flow rate was $1.2 \text{ m}^3 \text{ h}^{-1}$ and the applied power was 0.5 kW.

[43, 55, 56], the two-temperature Boltzmann distribution fitting was used. The ‘low’ rotational temperature was fitted using a group of states up to $J = 12$. The ‘high’ rotational temperature was fitted using a group of states $J \geq 16$ and $J \leq 23$, both of them considering the vibrational state zero. The resulting low and high rotational temperatures are shown in figure 11. The values of the higher of both temperatures are close to the reported ones for discharge with mist injection, respectively discharge in water [56, 57].

According to [55], the populations of low rotational states at fixed vibrational level are assumed to be in thermal equilibrium with the surrounding gas. Thus, the low rotational temperature can be used as an estimate of the gas temperature in the discharge channel. However, this has to be taken with caution, as was shown in [42, 43, 56]. The interpretation of the high rotational temperature is not so clear. This could be related to the different production mechanisms of OH radicals [56]. However, in the CaviPlasma system, there is also the process of cavitation collapse involved, which is reported to be able to produce OH radicals and is also capable of inducing light emission, called sonoluminescence [58, 59]. Considering the presence of all of these mechanisms in CaviPlasma dynamics, we could not distinguish between them.

In figure 11, the obtained vibrational temperature of OH(A-X) is also given. This temperature ranges from about 3000–4000 K and increases with the decrease in the channel length. According to [55], this temperature rather has the meaning of vibrational relaxation efficiency. However, if we also perform the estimation of excitation temperatures from hydrogen Balmer lines for our plasma system, according to [60], we can compare the obtained values and their dependency on the channel length (back-pressure).

$T_{\alpha\beta}$ for the H_α and H_β lines, and $T_{\beta\gamma}$ for the H_β and H_γ lines, respectively (see [60]), were estimated using Spectrum Analyzer 1.8 software [41]. The obtained $T_{\alpha\beta}$ values were in the range of 3700–4300 K and increased when the channel length decreased. If we compare the data obtained for $T_{\alpha\beta}$ with the values of T_{vibr} of OH(A-X) and their dependency on the length of the discharge channel (or back-pressure), see figure 11, they are in good agreement. $T_{\beta\gamma}$, considering only

the three largest discharge channels conditions at which the H_γ signal was sufficiently high, were about half the $T_{\alpha\beta}$ value. This indicates that the distribution of the excited state concentration in the studied glow state of our discharge is non-thermal (at least on the measured time-scale), if the assumptions and conclusions from [60] are valid also in our case.

3.3.3. ICCD camera study of discharge ignition and propagation.

The discharge ignition and propagation were studied using phase-resolved ICCD imaging. The study was performed for both tap and deionized water at two HCC lengths of 2 cm and 11 cm. The conductivity of the tap and deionized water was 0.5 mS cm^{-1} and $10 \mu\text{S cm}^{-1}$, respectively. The total water volume was 3 l and the water flow rate was $1.2 \text{ m}^3 \text{ h}^{-1}$ in both cases. The applied power was 0.46 kW for deionized water and 0.5 kW and 0.15 kW for tap water. The HV frequency was 65 kHz.

Phase-resolved imaging of the discharge evolution within one discharge period was performed by phase-locked gating of the ICCD camera using the triggering signal from the HV power supply. The intensity of the discharge emission for a 500 ns temporal window was relatively low, so the accumulated acquisition was necessary to achieve good signal-to-noise ratio. In order to estimate the effect of signal accumulation, a comparison of single-shot (non-accumulated) and $10\times$ accumulated phase-resolved imaging of CaviPlasma was performed. It was found that for $10\times$ accumulation, the spatial structure and discharge dynamics are similar to the single-shot images, while the low-light parts of the discharge are much better resolved (see the supplementary material, figure S4). Therefore, for the rest of the discussion, $10\times$ accumulated spatio-temporal maps will be used.

The results for deionized water are shown in figure 12 for short and long HCC conditions. The behaviour of the discharge is clearly seen for an 11 cm long HCC in figure 12(b). We can distinguish four discharge phases in each half-period:

- (i) At the beginning, the discharge length increases gradually with the increasing voltage. The current increase is slow.

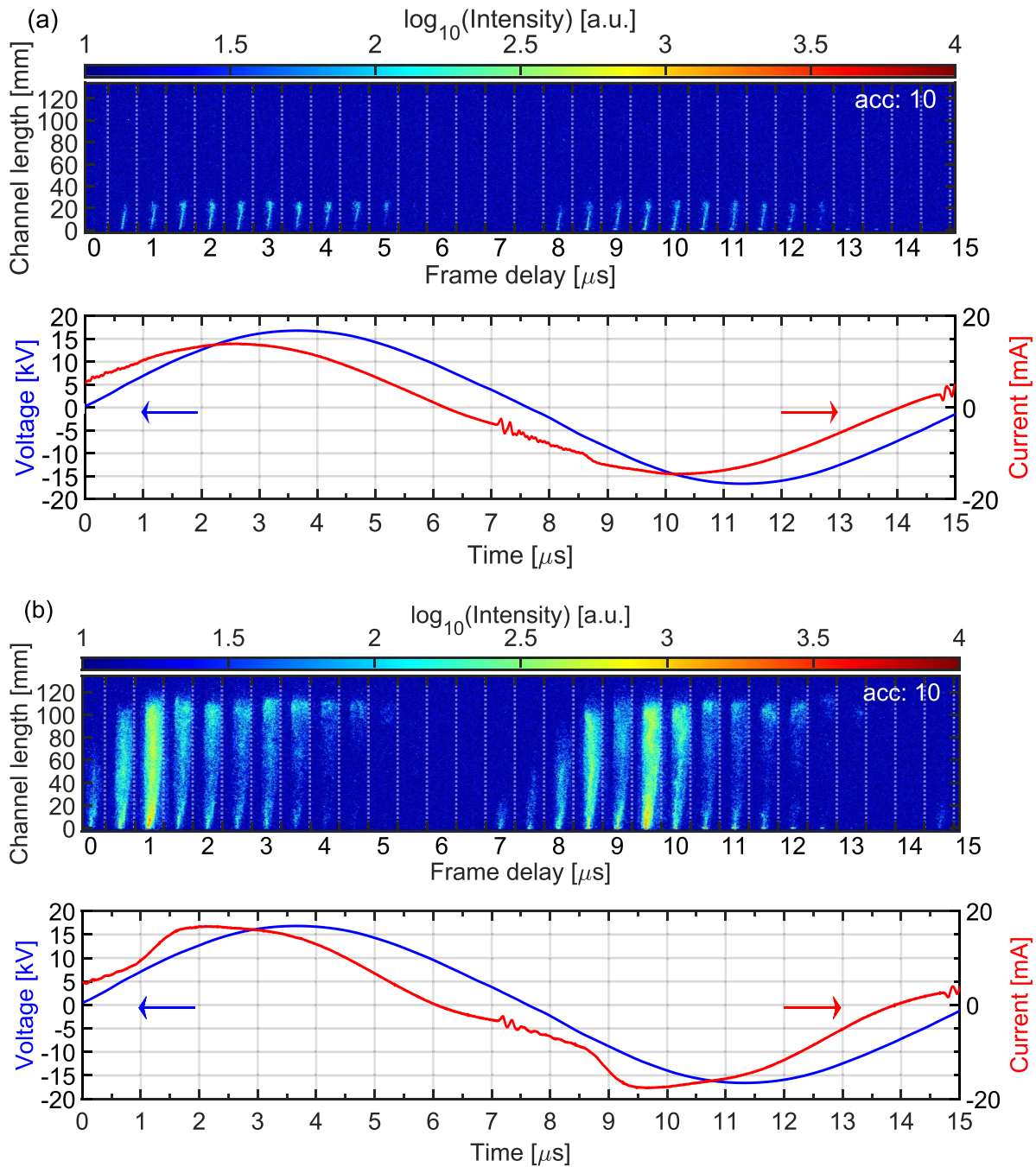


Figure 12. Phase-resolved time-sequence images of CaviPlasma in deionized water. Applied power 0.46 kW; HCC length (a) 2 cm, (b) 11 cm. Blue lines represent discharge voltage between electrodes, and red lines represent total current flowing through the discharge tube. The flow rate was $1.2 \text{ m}^3 \text{ h}^{-1}$ and the back-pressure was 100 kPa for 2 cm HCC length and 40 kPa for 11 cm HCC length, respectively.

- (ii) When the discharge column reaches the HCC end, a steep increase in discharge current occurs and the discharge emission intensity reaches its maximum.
- (iii) The discharge current and the discharge emission are almost steady until the discharge column starts to decay.
- (iv) In the decay phase, the discharge current also decreases.

The subsequent discharge half-periods differ depending on the voltage polarity. When the nozzle metal electrode is a cathode, the discharge current in phase (ii) increases more steeply and the cathode spots are also visible. When the HCC length is short, the discharge fills the whole HCC within a single step of our temporal resolution (500 ns); see figure 12(a).

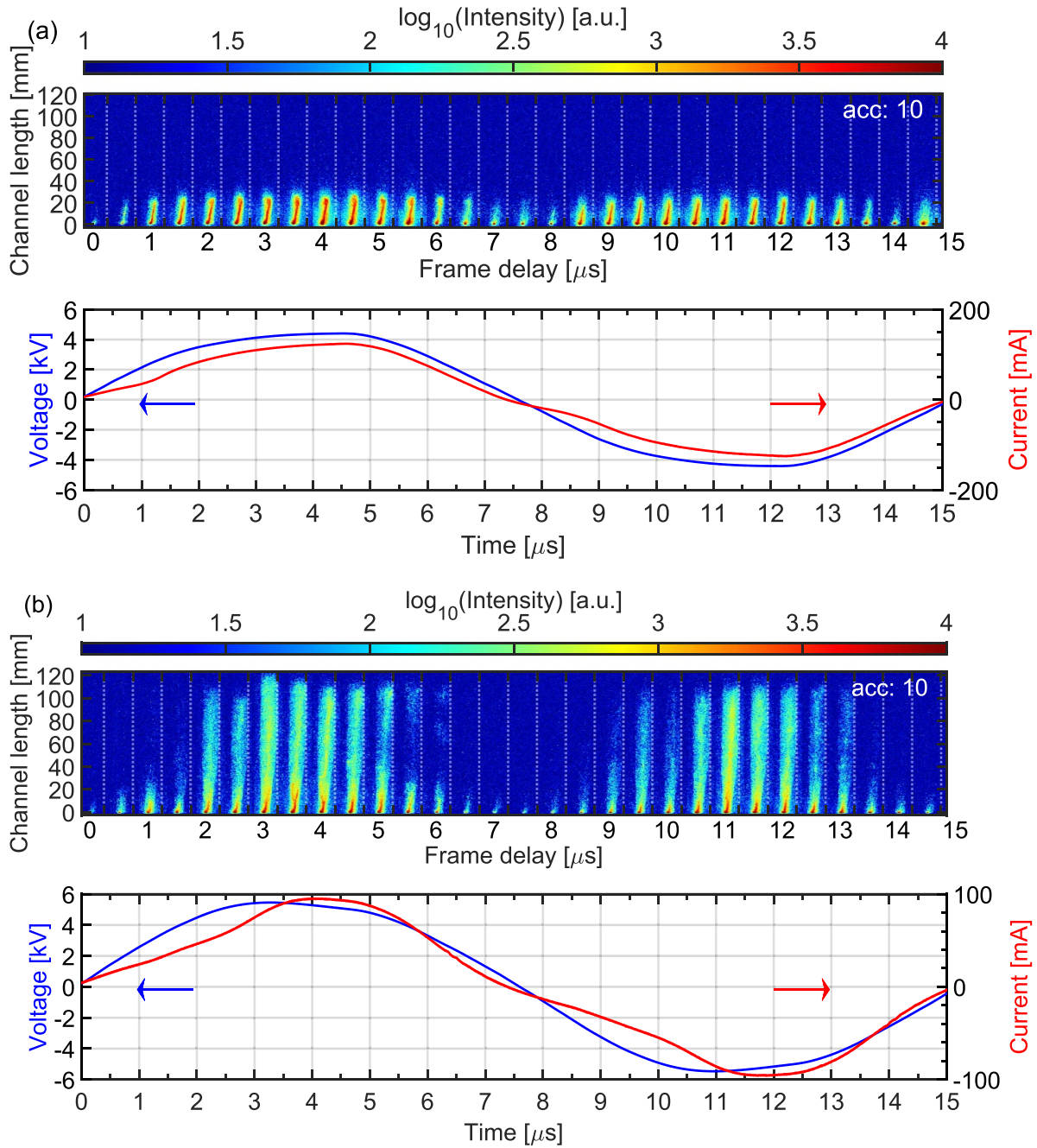


Figure 13. Phase-resolved time-sequence images of CaviPlasma in tap water. Applied power 0.5 kW; HCC length (a) 2 cm, (b) 11 cm. Blue lines represent discharge voltage between electrodes, and red lines represent total current flowing through the discharge tube. The flow rate was $1.2 \text{ m}^3 \text{ h}^{-1}$ and the back-pressure was 100 kPa for 2 cm HCC length and 40 kPa for 11 cm HCC length, respectively.

Images for tap water with an applied power of 0.5 kW are shown in figure 13.

In tap water, four phases of the discharge can also be identified. However, during the steady phase (iii) the discharge channel emission remains homogeneous for a longer time and in the decay phase (iv) the discharge column decays faster at the liquid electrode. The light emission is visible for almost the whole period.

The images for tap water at a much lower applied power of 0.15 kW are shown in figure 14. At such applied power, the

discharge can be generated in tap water only and the discharge emission is weaker and shorter than at the power of 0.5 kW.

The current–voltage waveforms for an 11 cm long HCC and for 0.5 kW applied power can be compared for deionized and tap water; see figures 12(b) and 13(b). Due to the higher conductivity of tap water, the current flowing through the discharge tube in the case of tap water is approximately six times higher than the current in the case of deionized water. The applied voltage is also substantially higher in the case of deionized water. These current–voltage waveforms were

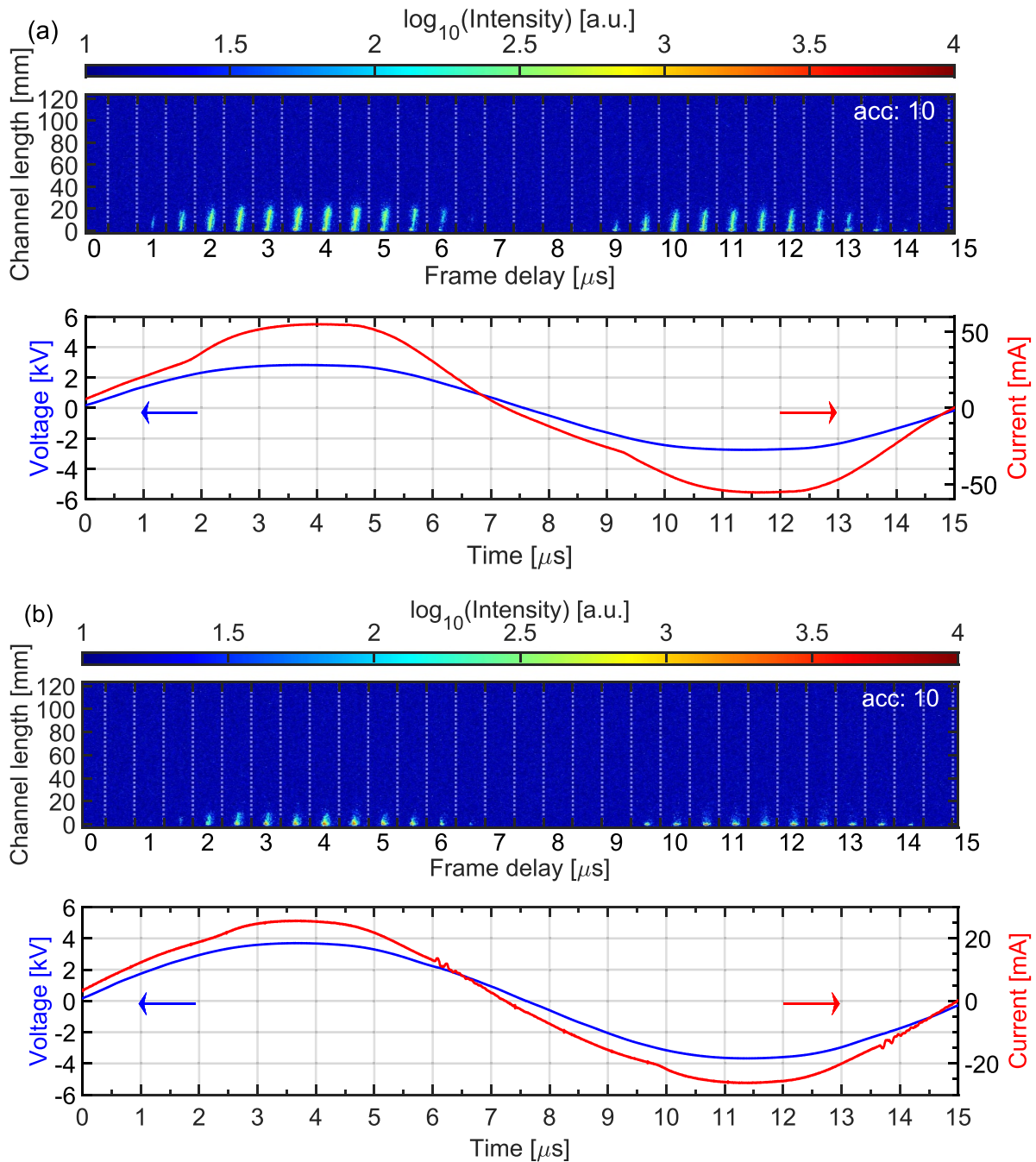


Figure 14. Phase-resolved time-sequence images of CaviPlasma discharge in tap water. Applied power 0.15 kW; HCC length (a) 2 cm, (b) 11 cm. Blue lines represent discharge voltage between electrodes, and red lines represent total current flowing through the discharge tube. The flow rate was $1.2 \text{ m}^3 \text{ h}^{-1}$ and the back-pressure was 100 kPa for 2 cm HCC length and 40 kPa for 11 cm HCC length, respectively.

integrated to obtain the power delivered to the discharge tube. The delivered power in the case of tap water was 0.24 kW and 0.12 kW in the case of deionized water. These so determined values are lower than the total applied power (0.5 kW). The estimated efficiency of the HV power supply is higher than 90%. As a result, the missing part of the applied power is dissipated due to current flowing through the branch of the water circuit with the pump.

3.4. Parametric study of hydrogen peroxide formation

The dependence of H_2O_2 production on the water flow rate, HCC length and treatment time was studied. There is a certain parametric window within which the required water flow rate at a specific HCC length can be set using combined control of the hydraulic pump driving frequency and the back-pressure at the water reservoir, maintaining a pressure difference in the

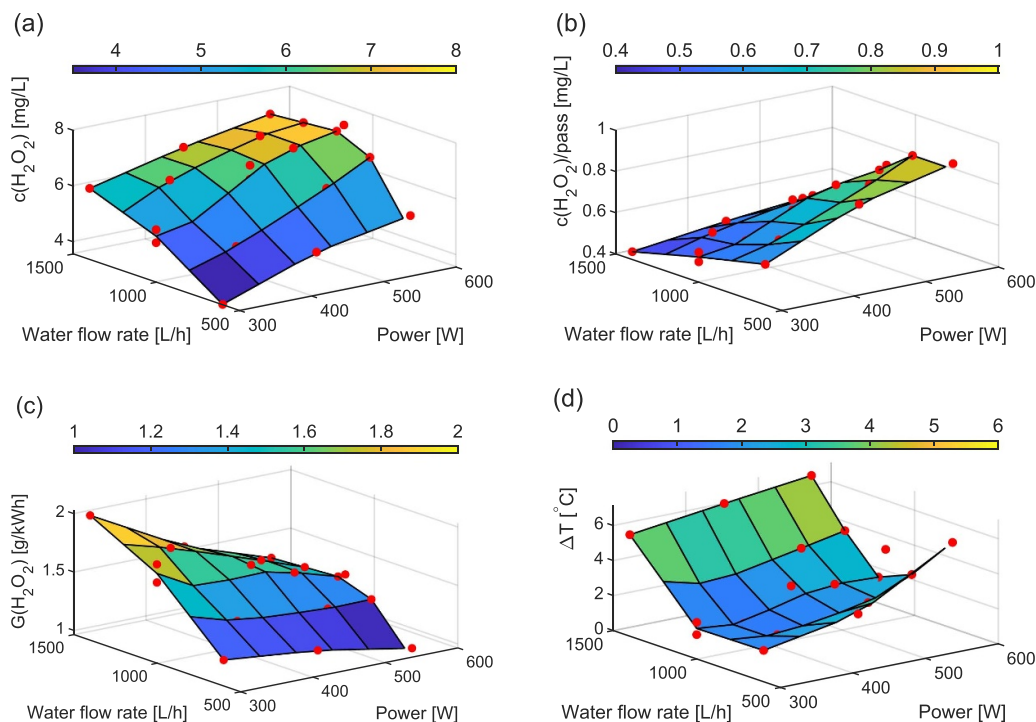


Figure 15. Parametric study of H₂O₂ production on HV power input and water flow rate: (a) concentration per fixed treatment time; (b) concentration per passage; (c) energy yield of H₂O₂ production; (d) water temperature increase. The red points show the results of experiments. The HCC length was kept at 4 cm. The treatment time was fixed to 90 s.

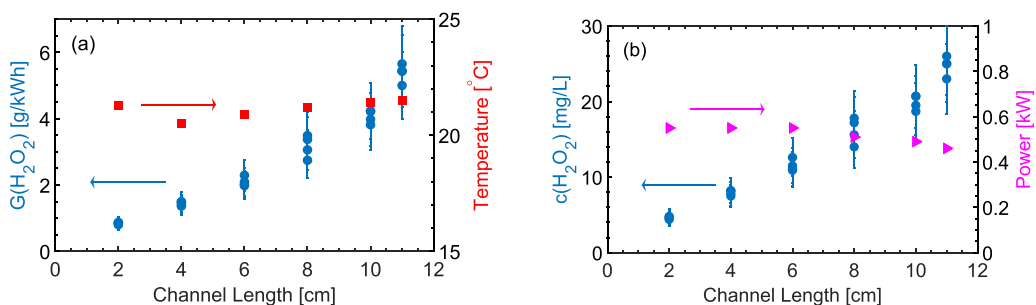


Figure 16. Parametric study of H₂O₂ production on HCC length. (a) Blue circles represent H₂O₂ energy yield, red squares represent water temperature. (b) Blue circles represent H₂O₂ concentration, magenta triangles represent the HV power input. The water flow rate was set to 1 m³ h⁻¹, and the treatment time was kept constant at 90 s. The HCC length was increased in 2 cm steps by reducing the back-pressure from atmospheric pressure down to 27 kPa.

reaction chamber. Similarly, for a given parametric window, a particular range of HCC lengths can be set while maintaining a specified flow rate.

A HV generator with a frequency of 64.5 kHz was used for these studies. The applied power was set to 0.5 kW. The used tap water (volume of 2.5 l) with initial temperature of 15 °C flowed through the system without discharge ignition for 90 s before each experiment. This treatment degassed the used water.

The influence of experimental conditions on the production of H₂O₂ was studied for the following parameters:

- (i) The influence of water flow rate and applied power. For the presented parametric window, the combined control of the flow rate (from 0.6 to 1.4 m³ h⁻¹) and back-pressure variation (from 26 kPa to 90 kPa) enabled the HCC length to be kept constant at 4 cm. The treatment time was kept fixed at 90 s for each experiment. The results are shown in figure 15. It can be seen that the H₂O₂ concentration increases with the increasing applied power, whereas the energy yield has a maximum at the lowest applied power and at the highest water flow rate.

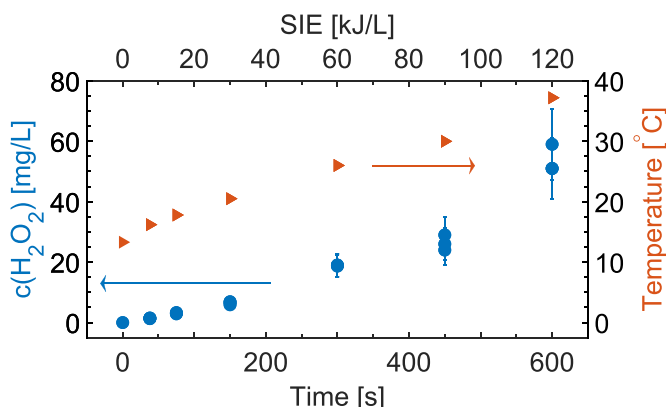


Figure 17. Parametric study of H_2O_2 production on exposure time. Blue circles represent H_2O_2 concentration, orange triangles represent water temperature. SIE means specific input energy. The HCC length was 2 cm at the water flow rate $1 \text{ m}^3 \text{ h}^{-1}$ and atmospheric pressure back-pressure.

- (ii) The influence of the HCC length. The water flow rate was set to $1 \text{ m}^3 \text{ h}^{-1}$, and the treatment time was kept constant at 90 s. The HCC length was varied by changing the back-pressure from atmospheric pressure down to 27 kPa. The results are shown in figure 16. The H_2O_2 energy yield and concentration increase with the increasing HCC length in this case.
- (iii) The influence of treatment time. For this experiment the following conditions were kept constant: the HCC length was 2 cm, the water flow rate was $1 \text{ m}^3 \text{ h}^{-1}$ and the back-pressure was atmospheric pressure. The treatment time was varied up to a maximum treatment time of 10 min, which corresponds to 62 passes through the HCC. The water temperature increases by 0.3°C per one pass through the system. The results are shown in figure 17. The H_2O_2 concentration gradually increases with the increasing treatment time, i.e. with the specific input energy (SIE), representing the amount of energy delivered to the unit volume of the treated liquid by the HV generator.

3.5. Key application parameters

Our previous research [11, 12] suggests that the key points for the applications of the CaviPlasma technology are the efficiency and production rate of reactive oxygen species (ROS). The final ROS product of the CaviPlasma water treatment is hydrogen peroxide (H_2O_2); however, even more reactive is the OH radical, which is a dominant precursor in the reaction paths of H_2O_2 production. In order to estimate the OH radical production and also the potential for further enhancement of ROS production, the following experiments were carried out in addition to the parametric study presented so far: (i) the estimation of OH production using TA and phenol

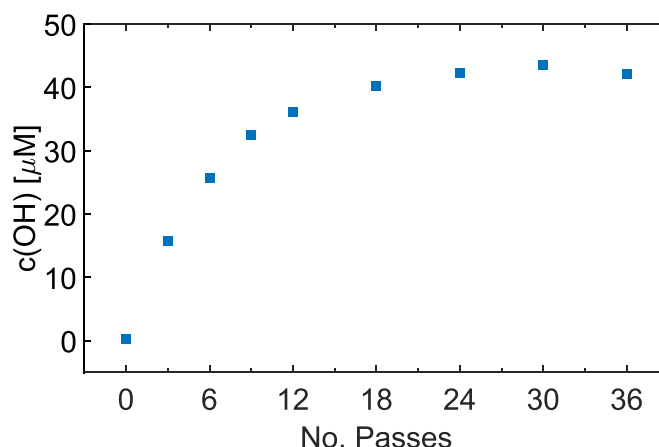


Figure 18. OH concentration evolution with number of passes. The flow rate of the solution through the active plasma zone was $1 \text{ m}^3 \text{ h}^{-1}$ and the HCC length was set to 8 cm using back-pressure reduction. Treatment was done in four 27 s steps representing three passes of 9 s each. Then the treatment steps were increased to 54 s. Power input was 0.7 kW at 50 kHz frequency.

acting as the chemical probes and (ii) re-setup of the hydraulic circuit in order to suppress the ohmic losses in the hydraulic circuit.

3.5.1. OH concentration study. The OH concentration was measured using the water solution of tTA as described in section 2.2. The flow rate of the solution through the active plasma zone was set to $1 \text{ m}^3 \text{ h}^{-1}$ and the HCC length was 8 cm for given conditions. The control sample was analyzed prior to the discharge operation with only the cavitation flow set on. The solution with the TA probe was treated for 180 s in the cavitation flow only. The conductivity and pH values of the solution prior to the plasma treatment were $460 \mu\text{S cm}^{-1}$ at 23°C and 10.3, respectively. The analysis of the chemical probe reveals only minor effects of the cavitation flow itself as the measured OH concentration was only $0.22 \mu\text{M}$. Then, the treatment with the discharge switched on was performed in four steps of 27 s each, representing three cycles of the whole solution volume treatment. Then, the next four steps of 54 s treatment time each were performed. The discharge was generated using an HV power supply with a power input of 0.7 kW at 50 kHz frequency.

The dependence of the OH concentration on the number of treatment cycles is shown in figure 18. The final decrease in OH concentration is probably due to destruction of monitored product (fluorescent 2-hydroxyterephthalic acid) in the discharge. When we compare the H_2O_2 production with the measured OH concentration, we see a considerable deficiency of the measured OH concentration with respect to the H_2O_2 concentration. Here we note that the reactions with the TA probe take place presumably in the liquid phase, while a

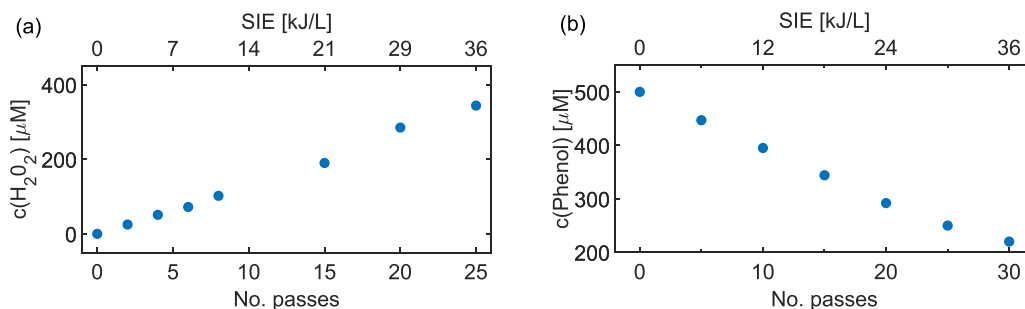


Figure 19. The dependencies of (a) H₂O₂ concentration and (b) phenol concentration on the number of passes of solution through the CaviPlasma and corresponding SIE. The flow rate was 1.44 m³ h⁻¹ and the HCC length was 5 cm. The power input was 0.57 kW at 50 kHz frequency. For H₂O₂ measurements (left), a dedicated apparatus was built with reduced dissipation of energy in the pump branch.

significant part of the H₂O₂ is probably produced in the gas phase—see e.g. [61]. The measured OH concentration then represents only a minor part of the total production of OH radicals in the form of solvated OH radicals that did not recombine to form the H₂O₂.

3.5.2. H₂O₂ yield and phenol oxidation. The experiments described here were performed at a flow rate of 1.44 m³ h⁻¹. The power supply frequency was 50 kHz and the applied power was set to 0.57 kW. The HCC length was 5 cm under the given conditions.

The H₂O₂ yield was measured in the first experiment. For this experiment, 8 l of tap water was used, the initial water conductivity was 510 μS cm⁻¹, the initial water pH was 7.24 and the initial water temperature was 26.2 °C. The pressure in the water tank was atmospheric. In this experiment, a dedicated apparatus with modified water circuit was built. In this case, the branch with the water pump was approximately four times longer than in the previous experiments described in this paper.

After all cycles, the water conductivity was 507 μS cm⁻¹, the water pH was 7.52 and the water temperature was 44 °C. The H₂O₂ measurements using the colorimetric method were performed regularly after 40 s of treatment, which corresponds to two passes of the whole treated volume. The dependence of the H₂O₂ concentration on the number of cycles is shown in figure 19. The energy yield for H₂O₂ production was calculated from these data. To enable direct comparison to data from the literature, only the HV power was considered for the energy yield calculations in this manuscript. The resulting energy yield was $G(\text{H}_2\text{O}_2) = 9.6 \text{ g kWh}^{-1}$ in this experiment. This value is four times higher than the value for the corresponding HCC length in figure 16. This is due to the reduced fraction of energy dissipated in the pump branch of the water circuit due to the reduced electrical conductivity of this part of the setup.

The degradation of phenol by CaviPlasma was also studied. Phenol removal using various plasma technologies has already been studied by many authors; see the review [30]. The phenol removal in the discharge in water is mainly due to the phenol reaction with OH radicals, so the phenol oxidation could serve as another estimate of OH concentration in the liquid.

The initial solution conductivity was 519 μS cm⁻¹ and the initial solution temperature was 23 °C. The solution was passed 30 times through the CaviPlasma and the back-pressure was set to 65 kPa. After each cycle, the solution was sampled and analyzed. After 30 cycles, the final conductivity of the solution was 694 μS cm⁻¹ and the solution temperature increased to 39 °C. The dependence of the phenol concentration on the number of cycles is shown in figure 19. The concentration of phenol decreased proportionally with the number of cycles, and the degradation obeyed first-order kinetics. The primary degradation products of the phenol were analyzed in parallel to the measurement of phenol degradation. Hydroquinone, catechol, 1,4-benzoquinone and hydroxy-1,4-benzoquinone were detected. These hydroxylated compounds are typical products of OH radical electrophilic attacks on the phenol ring, where OH is the expected reactive species in the plasma containing water vapour. The degradation efficiency of the phenol was $8 \times 10^{-9} \text{ mol J}^{-1}$ or 2.7 g kWh^{-1} , which is a rather high yield compared to that obtained from plasmas produced directly in water [30]. This also correlates with the higher yields of H₂O₂ obtained with the CaviPlasma setup.

The OH concentration can be estimated from the phenol concentration decrease and the rate coefficient for the reaction of phenol with OH radicals. The so-obtained OH concentration is 9.5 μM per pass, which is higher than the OH concentration obtained from the measurements with TA.

However, we also observe a deficiency of the measured OH concentration with respect to the H₂O₂ concentration. For the TA, for the phenol the reactions also take place presumably in the liquid phase. However, contrary to the TA probe, the direct oxidation products are measured using a phenol probe. The phenol probe measurements are therefore not affected by the anticipated TA (HTA) degradation in the active discharge zone. This is probably the reason for the higher OH concentration estimation using the phenol probe, but there could also be a reaction of phenol with ozone that was not considered.

4. Conclusions

AC glow discharge in a dense HCC with a Venturi nozzle with axial arrangement of electrodes in water has been studied at different discharge parameters: back-pressure, water flow rate and applied power. For a discharge powered by an AC power

source with a frequency of 65 kHz, the applied HV amplitude was 6 kV for tap water and 15 kV for deionized water when the flow rate was set to 1.2 m³ h⁻¹, the HCC length set to 11 cm and the electrodes were separated by 15.5 cm. The input power was typically 0.5 kW. The production of H, O and OH species in the discharge was proven by optical emission spectroscopy. The formation of H₂O₂ in water was determined by chemical methods. H₂O₂ concentrations of up to 60 mg l⁻¹ were produced, with an energy yield for H₂O₂ generation of 9.6 g kWh⁻¹ and a generation rate up to 2.4 g h⁻¹. These values of energy yield and generation rate belong to the highest values compared to other water treatment methods based on plasma processes, e.g. by using a diaphragm or pulsed gliding arc discharges; see the corresponding review [38]. The values of the energy yield range from 0.12 g kWh⁻¹ for the DC diaphragm discharge to 80 g kWh⁻¹ for the pulsed gliding arc discharge with water droplets. However, in this discharge, the production rate is only 0.02 g h⁻¹, which is a hundred times lower than the generation rate of CaviPlasma.

Moreover, the degradation of phenol admixture in water was studied and the obtained degradation efficiency of phenol was 2.7 g kWh⁻¹. Higher phenol degradation rates have only been reported in oxygen atmosphere at lower water flow rates (the highest value being 13 g kWh⁻¹ [62]).

CaviPlasma enables one of the highest water flow rates compared with other plasma–liquid systems. It should also be noted that the energy yields for CaviPlasma were calculated from the electrical power delivered to the experimental setup from the grid, and not only the energy dissipated in the plasma. Part of this power is lost in the pumps of the water circuit. Further research to decrease this lost power is in progress.



Data availability statement

All data that support the findings of this study are included within the article (and any supplementary files).

Acknowledgments

The Czech Science Foundation is gratefully acknowledged for its support of this research under Project No. GA22-11456S ‘Exploring fundamental interactions of hydrodynamic cavitation and low-temperature plasma to enhance the disinfection effects’. The research was supported also by the Technological Agency of Czech Republic under Project No. SS01020006 and by the Slovak Research and Development Agency under Project No. APVV-22-0247. J C was also supported by the Career Development Support Programme at the Faculty of Education, Masaryk University. The cooperation among the institutions was supported by CEEPUS network AT-0063. This work results within the collaboration of the COST Action CA19110.

ORCID iDs

J Čech  <https://orcid.org/0000-0002-4900-6011>
P Sťahel  <https://orcid.org/0000-0001-5078-6062>

D Trunec  <https://orcid.org/0000-0003-0210-5087>
P Rudolf  <https://orcid.org/0000-0003-2622-7898>
B Maršálek  <https://orcid.org/0000-0002-5559-2723>
E Maršálková  <https://orcid.org/0000-0002-7828-4037>
P Lukeš  <https://orcid.org/0000-0002-7330-0456>
A Lavrikova  <https://orcid.org/0000-0002-8510-6503>
Z Machala  <https://orcid.org/0000-0003-1424-1350>

References

- [1] Kausley S B, Dastane G G, Kumar J K, Desai K S, Doltade S B and Pandit A B 2019 *Clean Water for Developing Countries: Feasibility of Different Treatment Solutions* vol 10 2nd edn (Elsevier Inc.)
- [2] Jančula D, Mikula P, Maršálek B, Rudolf P and Pochylý F 2014 *Aquacult. Int.* **22** 509–21
- [3] Kozák J, Rudolf P, Hudec M, Štefan D and Forman M 2019 *ASME J. Fluids Eng.* **141** 041101
- [4] Rudolf P and Hudec M 2019 *Proc. 10th Int. Symp. on Cavitation (CAV 2018)* pp 211–5
- [5] Rudolf P, Kubina D, Hudec M, Kozák J, Maršálek B, Maršálková E and Pochylý F 2017 *EPJ Web. Conf.* **143** 02098
- [6] Rudolf P, Hudec M, Gríger M and Štefan D 2014 *EPJ Web. Conf.* **67** 02101
- [7] Maršálek B, Zezulka Š, Maršálková E, Pochylý F and Rudolf P 2020 *Chem. Eng. J.* **382** 122383
- [8] Zezulka Š E, F, Rudolf P and Hudec M B 2020 *J. Environ. Manage.* **255** 109862
- [9] Rudolf P, Pochylý F, Sťahel P, Ráhel J, Čech J and Maršálek B 2019 *Czech Patent* 308532
- [10] Rudolf P, Pochylý F, Sťahel P, Ráhel J, Čech J and Maršálek B 2021 Device for treatment of liquids and the method of treatment of liquids with use of this device WIPO PCT application No. WO2021/115498 (available at: <https://patentimages.storage.googleapis.com/38/b8/d5/efb582f2907fff/WO2021115498A1.pdf>)
- [11] Maršálek B, Maršálková E, Odehnalová K, Pochylý F, Rudolf P, Sťahel P, Ráhel J, Čech J, Fialová S and Zezulka Š 2020 *Water* **12** 8
- [12] Čech J, Sťahel P, Ráhel J, Prokeš L, Rudolf P, Maršálková E and Maršálek B 2020 *Water* **12** 1–18
- [13] Ihara S, Hirohata T, Kominato Y, Yamabe C, Ike H, Hakia K, Hirabayashi K and Tamagawa M 2014 *Electr. Eng. Japan* **186** 1–10 English translation of Denki Gakkai Ronbunshi
- [14] Bruggeman P J et al 2016 *Plasma Sources Sci. Technol.* **25** 053002
- [15] Machala Z, Tarabová B, Sersenová D, Janda M and Hensel K 2019 *J. Phys. D: Appl. Phys.* **52** 034002
- [16] Kaushik N K et al 2018 *Biol. Chem.* **400** 39–62
- [17] Brandenburg R et al 2019 *Plasma Process. Polym.* **16** 1–18
- [18] Thirumdas R, Kothakota A, Annapure U, Siliveru K, Blundell R, Gatt R and Valdramidis V P 2018 *Trends Food Sci. Technol.* **77** 21–31
- [19] Zhang Q, Ma R, Tian Y, Su B, Wang K, Yu S, Zhang J, Fang J 2016 *Environ. Sci. Technol.* **50** 3184–92
- [20] Lu P, Boehm D, Cullen P and Bourke P 2017 *Appl. Phys. Lett.* **110** 264102
- [21] Ito M, Oh J S, Ohta T, Shiratani M and Hori M 2018 *Plasma Process. Polym.* **15** 1700073
- [22] Gamaleev V, Iwata N, Ito G, Hori M, Hiramatsu M and Ito M 2020 *Appl. Sci.* **10** 801
- [23] Park H, Yoo S and Kim K 2019 *IEEE Trans. Plasma Sci.* **47** 1482–6
- [24] Yayci A, Baraibar A G, Krewing M, Fueyo E F, Hollmann F, Alcalde M, Kourist R and Bandow J E 2020 *ChemSusChem* **13** 2072–9

- [25] Mariotti D, Patel J, Švrček V and Maguire P 2012 *Plasma Process. Polym.* **9** 1074–85
- [26] Kaushik N K, Kaushik N, Linh N N, Ghimire B, Pengkit A, Sornsakdanuphap J, Lee S J and Choi E H 2019 *Nanomaterials* **9** 1–19
- [27] Lukes P and Locke B R 2005 *Ind. Eng. Chem. Res.* **44** 2921–30
- [28] Kozáková Z, Nejezchleb M, Krčma F, Halamová I, Čáslavský J and Dolinová J 2010 *Desalination* **258** 93–99
- [29] Magureanu M, Dobrin D, Mandache N B, Bradu C, Medvedovici A and Parvulescu V I 2013 *Plasma Process. Polym.* **10** 459–68
- [30] Jiang B, Zheng J, Qiu S, Wu M, Zhang Q, Yan Z and Xue Q 2014 *Chem. Eng. J.* **236** 348–68
- [31] Tampieri F, Giardina A, Bosi F J, Pavanello A, Marotta E, Zaniol B, Neretti G and Paradisi C 2018 *Plasma Process. Polym.* **15** 1700207
- [32] Galmiz O, Zemánek M, Pavliňák D and Černák M 2018 *J. Phys. D: Appl. Phys.* **51** 195201
- [33] Locke B R, Sato M, Sunka P, Hoffmann M R and Chang J S 2006 *Ind. Eng. Chem. Res.* **45** 882–905
- [34] Abramov V O, Abramova A V, Cravotto G, Nikonov R V, Fedulov I S and Ivanov V K 2021 *Ultrason. Sonochem.* **70** 105323
- [35] Abramov V et al 2022 *Processes* **10** 2063
- [36] Verdini F, Calcio Gaudino E, Canova E, Colia M C and Cravotto G 2023 *Ind. Eng. Chem. Res.* **62** 19311–22
- [37] Verdini F, Canova E, Solarino R, Calcio Gaudino E and Cravotto G 2024 *Environ. Pollut.* **342** 123041
- [38] Locke B R and Shih K Y 2011 *Plasma Sources Sci. Technol.* **20** 034006
- [39] Bobkova E S, Tatarinov A V, Ivanov E V and Gushchin P A 2018 *High Energy Chem.* **52** 171–82
- [40] Wang X, Tan Z, Han J and Li X 2020 *Plasma Sci. Technol.* **22** 115504
- [41] Navrátil Z, Trunec D, Šmíd R and Lazar L 2006 *Czech. J. Phys.* **56** 944–51
- [42] Voráč J, Synek P, Procházka V and Hoder T 2017 *J. Phys. D: Appl. Phys.* **50** 294002
- [43] Voráč J, Synek P, Potočňáková L, Hnilica J and Kudrle V 2017 *Plasma Sources Sci. Technol.* **26** 025010
- [44] Eisenberg G M 1943 *Ind. Eng. Chem. Anal. Ed.* **15** 327–8
- [45] Wagner W and Pruss A 1993 *J. Phys. Chem. Ref. Data* **22** 783–7
- [46] Flint E B and Suslick K S 1991 *Science* **253** 1397–9
- [47] Storey B D and Szeri A J 2000 *Proc. R. Soc. A* **456** 1685–709
- [48] Dular M and Coutier-Delgosha O 2013 *J. Fluid Mech.* **736** 44–66
- [49] Perrin L, Colombet D and Ayela F 2021 *Ultrason. Sonochem.* **70** 105277
- [50] Avtaeva S V, General A A and Kel'man V A 2010 *J. Phys. D: Appl. Phys.* **43** 315201
- [51] Kou L, Labrie D and Chylek P 1993 *Appl. Opt.* **32** 3531
- [52] Pope R M and Fry E S 1997 *Appl. Opt.* **36** 8710
- [53] Fry E S 2000 *Appl. Opt.* **39** 2743
- [54] Mason J D, Cone M T and Fry E S 2016 *Appl. Opt.* **55** 7163
- [55] Hart M 2019 *Publ. Astron. Soc. Pacific* **131** 015003
- [56] Bruggeman P, Schram D, González M A, Rego R, Kong M G and Leys C 2009 *Plasma Sources Sci. Technol.* **18** 025017
- [57] Tsumaki M and Ito T 2017 *AIP Adv.* **7** 1–8
- [58] Peng K, Qin F G, Jiang R, Qu W and Wang Q 2022 *Ultrason. Sonochem.* **88** 106067
- [59] Ohl C–D, Kurz T, Geisler R, Lindau O and Lauterborn W 1999 Bubble dynamics, shock waves and sonoluminescence *Phil. Trans. R. Soc. A* **357** 269–94
- [60] Edels H and Gambling W A 1959 *Proc. R. Soc. A* **249** 225–36
- [61] Gorbanev Y, O'Connell D and Chechik V 2016 *Chem. Eur. J.* **22** 3496–505
- [62] Grabowski L R 2006 Pulsed corona in air for water treatment *PhD Thesis Technische Universiteit Eindhoven*